Title

A Three-Dimensional Reconstruction Algorithm for Scanning Transmission Electron Microscopy Data from a Single Sample Orientation

Journal

Microscopy and Microanalysis, 28(5)

ISSN

1431-9276

Authors

Brown, Hamish G
Pelz, Philipp M
Hsu, Shang-Lin
et al.

Publication Date

2022-10-01

DOI

10.1017/s1431927622012090

Abstract

Increasing interest in three-dimensional nanostructures adds impetus to electron microscopy techniques capable of imaging at or below the nanoscale in three dimensions. We present a reconstruction algorithm that takes as input a focal series of four-dimensional scanning transmission electron microscopy (4D-STEM) data. We apply the approach to a lead iridate, $Pb_2Ir_2O_7$, and yttrium-stabilized zirconia, $Y_{0.095}Zr_{0.905}O_2$, heterostructure from data acquired with the specimen in a single plan-view orientation, with the epitaxial layers stacked along the beam direction. We demonstrate that Pb-Ir atomic columns are visible in the uppermost layers of the reconstructed volume. We compare this approach to the alternative techniques of depth sectioning using differential phase contrast scanning transmission electron microscopy (DPC-STEM) and multislice ptychographic reconstruction.

Key Words: Scanning transmission electron microscopy, Image reconstruction, Ptychography, Differential phase contrast (Received XX Y 20ZZ; revised XX Y 20ZZ; accepted XX Y 20ZZ)

A three-dimensional reconstruction algorithm for scanning transmission electron microscopy data from a single sample orientation

Hamish G. Brown,[1*] Philipp M. Pelz,[1,2] Shang-Lin Hsu,[1,2] Zimeng Zhang,[2] Ramamoorthy Ramesh,[2,3] Katherine Inzani,[4,5] Evan Sheridan,[4,5,6] Sinéad M. Griffin,[4,5] Marcel Schloz,[7] Thomas C. Pekin,[7] Christoph T. Koch,[7] Scott D. Findlay,[8] Leslie J. Allen,[9] Mary C. Scott,[1,2] Colin Ophus,[1] Jim Ciston[1]

[1] *National Center for Electron Microscopy Facility, Molecular Foundry, Lawrence Berkeley National Laboratory, Berkeley, California 94720, USA*

[2] *Department of Materials Science and Engineering, University of California, Berkeley, CA, 94720, USA*

[3] *Department of Physics, University of California, Berkeley, California 94720, USA.*

[4] *Materials Sciences Division, Lawrence Berkeley National Laboratory, Berkeley, California 94720, USA*

[5] *Molecular Foundry, Lawrence Berkeley National Laboratory, Berkeley, California 94720, USA*

[6] *Theory and Simulation of Condensed Matter, Department of Physics, King's College London, The Strand, London WC2R 2LS, UK.*

[7] *Department of Physics & IRIS Adlershof, Humboldt-Universität zu Berlin, Newtonstraße 15, 12489 Berlin, Germany*

[8] *School of Physics and Astronomy, Monash University, Victoria 3800, Australia*

---

[*] Current address: Ian Holmes Imaging Centre, Bio21 Molecular Science and Biotechnology Institute, the University of Melbourne, Parkville, Victoria 3052, Australia.

[9]*School of Physics, University of Melbourne, Parkville, Victoria 3010, Australia*
Corresponding Authors: Hamish G Brown <hgbrown@unimelb.edu.au>, Colin Ophus <clophus@lbl.gov>, Jim Ciston <jciston@lbl.gov>

Introduction

There has recently been significant interest in nanoscale three-dimensional materials such as polarization vortices in layered $PbTiO_3$-$SrTiO_3$ heterostructures (Yadav et al., 2016), van der Waals heterostructures (Withers et al., 2015) and strain-engineered nanoparticles (Oh et al., 2020). Development of these materials is facilitated by imaging techniques capable of three-dimensional characterisation at nanometer resolution. However, three dimensional imaging techniques such as electron tomography (Yang et al., 2017b) and current optical sectioning methods in scanning transmission electron microscopy (STEM) (van Benthem et al., 2006; Xin & Muller, 2009) typically rely on high-angle annular dark-field (HAADF) STEM which is often only sensitive to the heavy atoms within the sample.

Techniques which reconstruct the electric potential of a sample from diffraction plane measurements of the modification of the electron probe after transmission through the specimen, such as differential phase contrast (DPC) STEM (Shibata et al., 2017) and STEM ptychography (Nellist et al., 1995; Yang et al., 2016; Jiang et al., 2018b), are alternatives that are sensitive to both light and heavy atoms. The take-up of these techniques has been accelerated by recent advances in segmented detectors (Shibata et al., 2010) and the 4D-STEM technique – where full two dimensional diffraction patterns are recorded for a two dimensional raster scan of a STEM probe. The latter has been enabled by advanced electron cameras capable of reading out full diffraction patterns at frequencies of the order of 100s of Hertz or greater, approaching the typical dwell times of a focused STEM probe, which typically vary from tens of μs to a few ms (Ophus, 2019).

In their most common implementations, ptychography and DPC assume that electron beam-sample interaction occurs in a single spatial plane – referred to as the projection or phase object approximation – a theoretical framework that is inconsistent with atomic resolution imaging of crystalline materials more than a few nanometer thick. Not withstanding the underlying projection approximation, DPC and phase object ptychography have both been usefully applied for three-dimensional imaging. Since the final reconstruction is most sensitive to features close to where the beam comes to a focus, three dimensional information can be intuited from a DPC focal series of a specimen (Bosch & Lazić, 2019). Information about the three dimensional structure of a specimen has been demonstrated in single-sideband ptychography (SSB) (Yang et al., 2016) by varying in the reconstruction the z coordinate of the single spatial plane at which beam-specimen interaction is assumed to have occurred.

Multislice ptychography, an extension of the ptychography technique that will be used as a standard of comparison in this paper, has been proposed as a solution to the limitations of phase-object based ptychography. Here depth-wise propagation and multiple scattering of the illumination are taken into account by assuming that the illumination interacts with the sample at n distinct depth (z) separated planes (Maiden et al., 2012). Though numerical stability of the algorithm remains problematic, requiring careful parameter selection and regularization (Jiang et al., 2018a), electron multislice ptychographic reconstruction has been demonstrated in experiment to improve in-plane resolution and reconstruction fidelity of thick materials (Schloz et al., 2020; Chen et al., 2021) relative to phase-object based ptychography. Optical sectioning of a carbon nanotube sample with nanotubes located at different depths (Gao et al., 2017) has also been shown with the technique, demonstrating its promise as a three-dimensional reconstruction technique.

This paper focuses on a three-dimensional imaging technique capable of visualizing both light and heavy atoms in a thick sample with nanoscale depth selectivity. We reconstruct from a focal series of 4D-STEM measurements the scattering matrix ($\mathcal{S}$-matrix), a mathematical formalism common in quantum scattering theory (Weinberg, 1995) for calculating the phase and intensity of the scattered wave from a known input wave and that is capable of describing multiple electron scattering in an electron microscopy sample (Sturkey, 1962). We then use this $\mathcal{S}$-matrix to synthesize images of the specimen at different focal planes. We apply this technique to a lead iridate, $Pb_2Ir_2O_7$ (PIO), and yttrium-stabilized zirconia, $Y_{0.095}Zr_{0.905}O_2$ (YSZ), heterostructure and demonstrate that Pb-Ir atomic columns are visible in the uppermost layers of the reconstructed volume. This builds on previous work (Spence, 1998; Allen et al., 2000; Findlay, 2005; Brown et al., 2018; Donatelli & Spence, 2020) on $\mathcal{S}$-matrix retrieval that focused on single crystal structures. We compare results with a DPC-STEM focal series, phase-object ptychography and multislice ptychography. For the case presented, only $\mathcal{S}$-matrix reconstruction led to identification of the Pb-Ir columns, which are identified by caldera-like features characteristic of heavy atoms in phase contrast reconstruction.

Materials and methods

Theory of $\mathcal{S}$-matrix reconstruction

For a brief derivation of the $\mathcal{S}$-matrix formalism we take as our starting point the Schrödinger equation in reciprocal space for the electron wavefunction with a relativistic velocity along the z-direction, for which the paraxial approximation is appropriate. On a discretized grid with periodic boundary conditions [1], this equation is given by (Coene & Van Dyck, 1990)

$$\frac{\partial \psi_{\mathbf{g}}}{\partial z} = -i\pi\lambda g^2 \psi_{\mathbf{g}}(z) + \sum_{h} i\sigma V_{\mathbf{g}-\mathbf{h}}(z)\psi_{\mathbf{h}}(z)\,. \tag{1}$$

Here the Fourier coefficients of the electron wavefunction are given by $\psi_{\mathbf{g}}$ for reciprocal space coordinate $\mathbf{g}$ with amplitude g, λ is the electron wavelength, σ is the interaction constant[2] in radians/V and $V_{\mathbf{g}-\mathbf{h}}(z)$ are the 2D Fourier coefficients of the projected electrostatic potential at each depth z in the sample. From Eq. (1) we can construct a matrix first-order differential

---

[1] This is exact for a crystal and a good approximation for a non-periodic object if the field of view is sufficiently large in real space.

[2] The interaction constant is given by $\sigma = 2\pi m_e e\lambda/h^2$ where m_e, e and h are the mass of an electron, the charge of an electron and Planck's constant respectively.

equation,

$$\frac{\partial \boldsymbol{\psi}(z)}{\partial z} = i\mathcal{A}(z)\boldsymbol{\psi}(z), \tag{2}$$

where $\boldsymbol{\psi}$ is a column vector containing the Fourier coefficients of the electron wavefunction. We write the entries of the matrix $\mathcal{A}$, the structure matrix, for an entry corresponding to the Fourier coefficient $\mathbf{g}$ of the scattered electron wave and Fourier coefficient $\mathbf{h}$ of the incoming electron wavefunction as,

$$\mathcal{A}_{\mathbf{g},\mathbf{h}}(z) = -\pi\lambda g^2\delta_{\mathbf{g}-\mathbf{h}} + \sigma V_{\mathbf{g}-\mathbf{h}}(z). \tag{3}$$

In the absence of any scattering potential (i.e. $V_{\mathbf{g}-\mathbf{h}}(z) = 0$) the diagonal terms, $-\pi\lambda g^2\delta_{\mathbf{g}-\mathbf{h}}$, where $\delta_{\mathbf{g}-\mathbf{h}}$ is the Kronecker delta, have an equivalent effect to the Fresnel free-space propagator. If, on the other hand, the terms $-\pi\lambda g^2$ are ignored then Eq. (3) can be shown to reduce to the phase object approximation. Taking both sets of terms together, Eq. (3) encapsulates the simultaneous probe-specimen interaction (via V) and propagation that leads to the phenomenon colloquially referred to as "dynamical diffraction."

A standard solution to Eq. (3) is the $\mathcal{S}$-matrix solution,

$$\boldsymbol{\psi}(z + \Delta z) = e^{i\Delta z\mathcal{A}(z)}\boldsymbol{\Psi}(z) = \mathcal{S}(\Delta z)\boldsymbol{\Psi}(z)\,. \tag{4}$$

It is implicitly assumed in Eq. (4) that $V_{\mathbf{g}-\mathbf{h}}(z)$ is constant over thickness Δz. Where $V_{\mathbf{g}-\mathbf{h}}(z)$ varies with thickness, the $\mathcal{S}$-matrix can be constructed as a product of $\mathcal{S}$-matrices over n thinner sub-regions within which the z variation of $V_{\mathbf{g}-\mathbf{h}}(z)$ is minimal,

$$\mathcal{S}(z) = \prod_{i=0}^{n-1} \mathcal{S}(z_{i+1} - z_i). \tag{5}$$

In a 4D-STEM experiment the diffraction pattern for each raster scan position of a focused probe is measured and, for a probe position $\mathbf{R}$ and diffraction coordinate $\mathbf{g}$, this diffraction pattern can be calculated using the $\mathcal{S}$-matrix as

$$I(\mathbf{g},\mathbf{R},\Delta f) = \left|\sum_{\mathbf{h}} \mathcal{S}_{\mathbf{g},\mathbf{h}} A(\mathbf{h}) e^{-2\pi i\mathbf{h}\cdot\mathbf{R} - i\pi\lambda h^2 \Delta f - i\chi(\mathbf{h})}\right|^2 . \tag{6}$$

Here Δf is the probe defocus relative to the entrance surface of the specimen and $A(\mathbf{h})$ is the aperture function, a top-hat function that is 1 for Fourier components within the aperture, $|\mathbf{h}| < h_{\max} = \alpha/\lambda$ (α is the probe convergence semi-angle in radians), and 0 otherwise. The quantity $\chi(\mathbf{h})$ is the aberration function, if aberration coefficients for the probe forming lens are known a-priori they can be incorporated into the reconstruction. This was not the case for results presented in this manuscript. We seek to recover the complex-valued $\mathcal{S}$-matrix for a set of real-valued 4D-STEM datasets $I(\mathbf{g},\mathbf{R},\Delta f)$ recorded for a number of scan positions $\mathbf{R}$ and defoci Δf, a phase retrieval problem which we solve using a gradient descent approach (Guizar-Sicairos & Fienup, 2008; Thibault & Guizar-Sicairos, 2012; Wang et al., 2017; Pelz et al., 2021), see Algorithm 1.

Depth sectioning from the $\mathcal{S}$-matrix

The specimen potential $V(x, y, z)$ would ideally be directly retrieved from the $\mathcal{S}$-matrix resulting from the phase-retrieval step, and previous work has identified a quantitative method of doing this for a perfect crystalline sample (Spence, 1998; Allen et al., 2000; Donatelli & Spence, 2020) and demonstrated the technique experimentally (Brown et al., 2018). Here we consider the general case of a more heterogeneous sample such as a heterostructure or nanoparticle and we use an optical sectioning approach that estimates the potential at a given depth of the object (Ophus et al., 2019).

Consider $\mathcal{S}_{\mathbf{r},\mathbf{h}}$ (the $\mathcal{S}$-matrix component that maps plane wave input $\mathbf{h}$ to a real-space exit surface wavefunction [3]) for the case indicated in Fig.1(a), freespace propagation through

---

[3] The $\mathcal{S}$-matrix is a mathematical construct common in quantum physics that maps the input momentum states (i.e. Fourier components of the wavefunction) of the incoming particle to the output momentum states (Weinberg, 1995). In this paper we often use a mixed momentum and real space representation of

Algorithm 1 $\mathcal{S}$-matrix retrieval from a 4D-STEM dataset via gradient descent using an amplitude difference cost function Wang et al. (2017); Pelz et al. (2021)

```
Input:
4D-STEM datasets $I(\mathbf{g}, \mathbf{R}, \Delta f)$, with pixel dimensions $(g_x, g_y, R_x, R_y, n_{\Delta f})$. We denote the total number of scan positions across all defoci $N_{\mathbf{R}_i,\Delta f}$
Lens defoci $\Delta f$ in units of length
Probe positions $\mathbf{R}$ in units of length
Probe forming aperture $g_\alpha$ in units of inverse length
$\mu$, the algorithm "step size"
Initialize :
Calculate reconstruction grid dimensions $(M_x/\Delta g_x, M_y/\Delta g_y)$, where $M_i = \mathrm{ceil}(\max(R_i) - \min(R_i))\Delta g_i$ for $i = x, y$, $\Delta g_i$ is the diffraction pixel size in units of inverse length and ceil is the ceiling function.
Initialize $\mathcal{S}$-matrix : $\mathcal{S}_{\mathbf{g},\mathbf{h}} = \delta_{\mathbf{g}-\mathbf{h}}$, where the the input Fourier coefficients are those that sit within the probe forming aperture, $\{\mathbf{h} : |\mathbf{h}| < g_\alpha\}$.
Calculate illumination matrix for each probe position and defocus, $\psi_{\mathbf{h},\{\Delta f,\mathbf{R}\}}(0) = Ae^{2\pi i\mathbf{R}\cdot\mathbf{h} - i\pi h^2\lambda\Delta f - i\chi(\mathbf{h})}$, incorporating aberration coefficients (if known). The quantity $A$ is the mean diffraction pattern amplitude in the 4D-STEM dataset $A = \sqrt{\sum_{\Delta f,\mathbf{R}} I(\mathbf{g}, \mathbf{R}, \Delta f)/n_{\Delta f}/R_x/R_y}$
Run:
  for l = 0 to L do {Loop over amplitude flow iterations}
    for $\mathbf{R}_i$, $\Delta f_i$ in $\{\mathbf{R}, \Delta f\}$ do {Loop over scan postions and defoci in dataset}
      $\hat{\Psi}(\mathbf{g}, \mathbf{R}_i, \Delta f_i) = \sum_{\mathbf{h}} \mathcal{S}_{\mathbf{g},\mathbf{h}} \psi_{\mathbf{h},\{\mathbf{R}_i,\Delta f_i\}}$ {Forward operation}
      $\hat{\Psi}(\mathbf{g}, \mathbf{R}_i, \Delta f_i) = \hat{\Psi}(\mathbf{g}, \mathbf{R}_i, \Delta f_i) - I(\mathbf{g}, \mathbf{R}_i, \Delta f_i) \cdot \hat{\Psi}(\mathbf{g}, \mathbf{R}_i, \Delta f_i)/|\hat{\Psi}(\mathbf{g}, \mathbf{R}_i, \Delta f_i)|$
      $\mathcal{S}_{\mathbf{g},\mathbf{h}} -= \mu/N_{\Delta f,\mathbf{R}_i} \hat{\Psi}(\mathbf{g}, \mathbf{R}_i, \Delta f_i) \otimes_{\text{outer}} \psi^*_{\mathbf{h},\mathbf{R}_i,\Delta f_i}$ {Back-projection (adjoint) operation}
    end for
  end for
```

distance z_0, phase object interaction with potential (e.g. an atom), and further propagation through distance $\Delta z = z_1 - z_0$,

$$\mathcal{S}_{\mathbf{r},\mathbf{h}} = \mathcal{P}(\mathbf{r}, \Delta z) \otimes_{\mathbf{r}} \left[e^{i\sigma V(\mathbf{r})} e^{-i\pi\lambda h^2 z_0} e^{2\pi i \mathbf{h}\cdot\mathbf{r}} \right] . \tag{7}$$

Here $\mathcal{P}(\mathbf{r}, z)$ is the real space representation of the Fresnel free space propagator for propagation of distance z and the potential for the atom $V(\mathbf{r})$ is assumed projected (ie. depth integrated). Using the convolution theorem, Eq. (7) can be written as the inverse Fourier transform of the product of the Fourier transforms of the individual expressions:

$$\mathcal{S}_{\mathbf{r},\mathbf{h}} = e^{-i\pi\lambda z_0 h^2} \int e^{-i\pi\lambda\Delta z g^2} \hat{T}_{\mathbf{g}-\mathbf{h}} e^{2\pi i \mathbf{g}\cdot\mathbf{r}} d\mathbf{g} \, , \tag{8}$$

where we have defined $\hat{T}_{\mathbf{g}} = \mathcal{F}_{\mathbf{r}\to\mathbf{g}} \left\{ e^{i\sigma V(\mathbf{r})} \right\}$ and made use of the Fourier shift theorem. Making the change of variable $\mathbf{g} \to \mathbf{g} + \mathbf{h}$, Eq. (8) becomes

$$\mathcal{S}_{\mathbf{r},\mathbf{h}} = e^{-i\pi\lambda z_0 h^2} \int e^{-i\pi\lambda\Delta z (\mathbf{g}+\mathbf{h})^2} \hat{T}_{\mathbf{g}} e^{2\pi i (\mathbf{g}+\mathbf{h})\cdot\mathbf{r}} d\mathbf{g} \, , \tag{9}$$

$$= e^{2\pi i \mathbf{h}\cdot\mathbf{r} - i\pi\lambda z_1 h^2} \int e^{-i\pi\lambda\Delta z g^2} \hat{T}_{\mathbf{g}} e^{2\pi i \mathbf{g}\cdot(\mathbf{r} - \lambda\Delta z \mathbf{h})} d\mathbf{g} \, . \tag{10}$$

Invoking the convolution theorem and Fourier shift theorem again (in reverse form to that used previously), this becomes,

$$\mathcal{S}_{\mathbf{r},\mathbf{h}} = e^{2\pi i \mathbf{h}\cdot\mathbf{r} - i\pi\lambda z_1 h^2} \left[\mathcal{P}(\mathbf{r}, \Delta z) \otimes_{\mathbf{r}} e^{i\sigma V(\mathbf{r} - \mathbf{h}\lambda\Delta z)} \right] . \tag{11}$$

For this case, the $\mathcal{S}$-matrix consists of the atom with a lateral shift of $\mathbf{h}\lambda\Delta z$ and free-space propagation of Δz [schematically shown in Fig. 1(a)] with a multiplicative phase ramp $e^{2\pi i \mathbf{h}\cdot\mathbf{r}}$. To generate our optical section reconstruction at depth z, we apply the inverse of each of these processes (i.e. the phase ramp, propagation and paraxial shift) for each $\mathbf{h}$ in $\mathcal{S}_{\mathbf{r},\mathbf{h}}$, sum $\mathcal{S}_{\mathbf{r},\mathbf{h}}$ over

---

this quantity which is related to the more conventional representation of the $\mathcal{S}$-matrix via an inverse Fourier transform operation ($\mathcal{S}_{\mathbf{r},\mathbf{h}} = \mathcal{F}^{-1}_{\mathbf{g}\to\mathbf{r}} \mathcal{S}_{\mathbf{g},\mathbf{h}}$).

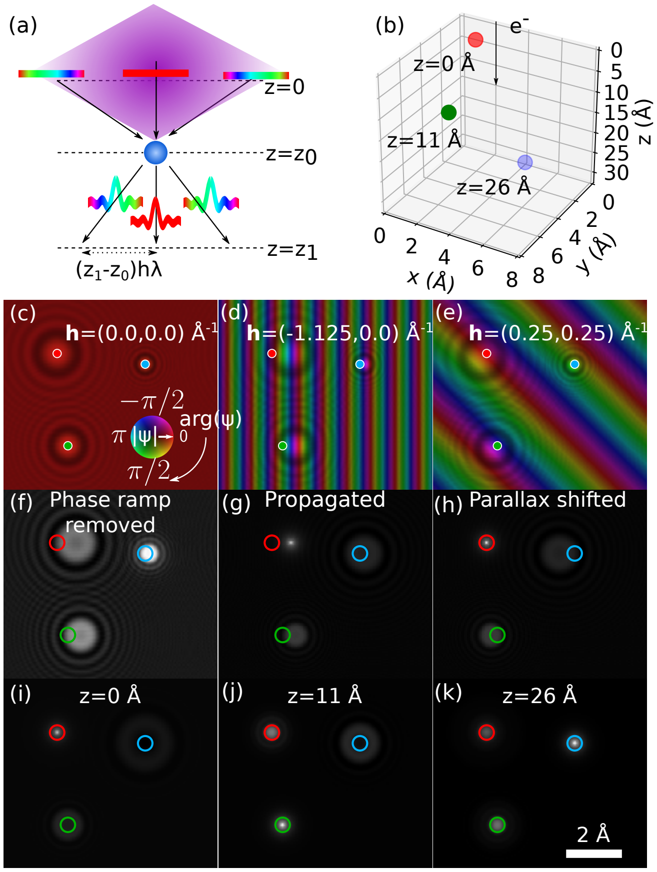

Fig. 1. Reconstructing three dimensional information from the $\mathcal{S}$-matrix. (a) For an atom at depth z_0, each component of the $\mathcal{S}$-matrix will acquire a phase through interaction with this atom. For a toy model system of three oxygen atoms at different points in 3D space as shown in (b) the complex $\mathcal{S}$-matrix components for three different Fourier component inputs $\mathbf{h}$ are shown in (c-e). The phase of the wavefunction is given by hue (color) and intensity by the lightness as indicated by the color-wheel in (c). The reconstruction method described in the text involves (f) removing the phase ramp, (g) propagating the complex wavefunction back to the plane of interest and (h) correcting the parallax shift from propagation. Only the phase is plotted in gray-scale in these and following panels. Shown in (i)-(k) are the reconstructions for the respective planes of the different atoms.

all $\mathbf{h}$ and the phase of the result should be a reasonable approximation to $V(\mathbf{r})$. Averaging over the different momentum components $\mathbf{h}$ of the STEM probe provides some robustness against the effects of multiple scattering, although it is not addressed explicitly in the depth sectioning part of the algorithm. This is analagous to the diminution of dynamical effects observed as a result of averaging diffraction patterns over different beam tilts in the precession electron diffraction technique (Ciston et al., 2008).

Although the algorithm will be applied to a strongly scattering crystalline sample later in the paper, for clarity of explanation we will first demonstrate the algorithm on a simulated $\mathcal{S}$-matrix of a toy model consisting of three weakly scattering oxygen atoms at different depths as shown in Fig. 1(b). Forward simulated $\mathcal{S}$-matrix components for different Fourier components $\mathbf{h}$ are shown in Fig. 1(c-e). The phase of the wavefunction is given by hue (color) and wavefunction intensity by the lightness as indicated by the color-wheel in (c). The positions of the atoms projected onto the 2D plane are indicated with colored dots and the paraxial shift from the projected positions of each of these atoms is visible. Shown in the next row of Fig. 1, with now just the phase plotted in gray color scale, are first the removal of the phase ramp $e^{2\pi i\mathbf{h}\cdot\mathbf{r}}$ in (f), the application of the propagation operator $\mathcal{P}(\mathbf{r}, -32\text{ Å})$ in (g) and finally, in (h), the correction of the paraxial shift $\lambda(z_1 - z_0)\mathbf{h}$ to reconstruct the atom at nominal height $z = 0$ from Fig. 1(b). These steps are applied to all components of $\mathcal{S}_{\mathbf{r},\mathbf{h}}$ and summed over all $\mathbf{h}$, which as can be seen in Fig. 1(i) further diminishes the contributions of atoms at different depths to the plane of reconstruction. The process is repeated for the other two atoms in Fig. 1(j) and (k). The high spatial resolution exhibited in these reconstructions is the result of their reconstruction from a forward simulated $\mathcal{S}$-matrix – finite signal-to-noise and partial coherence of the STEM probe will limit the fidelity of reconstruction in the experimental case. For the case where this algorithm is applied to a thick crystal containing heavy elements, multiple electron scattering means that Eq. (8) is not strictly valid. Optical sections will be perturbed by scattering of the beam at other depths within the sample. We expect the algorithm to be somewhat robust to these effects due to the averaging of multiple scattering matrix component in reconstruction.

Multislice ptychography

In the formalism of ptychography, the phase object approximation is usually applied to the Schrödinger equation and the probe-specimen interaction is sufficiently described for thin specimens in the absence of dynamical scattering. A single 2D slice $V(r_{x,y})$, onto which the specimen potential is projected along the z-axis, can then be reconstructed by the ptychographic reconstruction algorithm of choice. For thick specimens that involve multiple scattering the projection approximation breaks down and reconstruction quality deteriorates. Multislice ptychography aims to circumvent these issues. Probe-specimen interaction is modelled by the multislice algorithm, a split step solution to the Schrödinger equation for a fast electron, Eq. (1), where the specimen potential is projected into N distinct slices, as in Eq. (5). Propagation and transmission operations are applied sequentially within those slices and an iteration of the multislice algorithm to advance the real space wavefunction $\psi_n(\mathbf{r_{x,y}})$ from slice n to slice $n+1$ may be written:

$$\psi_{n+1}(\mathbf{r_{x,y}}) = \mathcal{P}(\mathbf{r_{x,y}}, \Delta z) \otimes_{\mathbf{r_{x,y}}} \left(\psi_n(\mathbf{r_{x,y}}) e^{i\sigma V_n(\mathbf{r_{x,y}})}\right) . \tag{12}$$

From the various existing ptychographic reconstruction algorithms that use the multislice method to recover the potential of a thicker specimen, we consider a gradient based algorithm with a Polak-Ribière conjugate gradient optimization method. Here, a loss function is formed and iteratively minimized in the search direction that is guided by its gradients. The partial derivatives, required to generate the gradients, are efficiently calculated by backpropagation of the loss function. A more detailed description of the ptychographic reconstruction algorithm is given in Schloz et al. (2020).

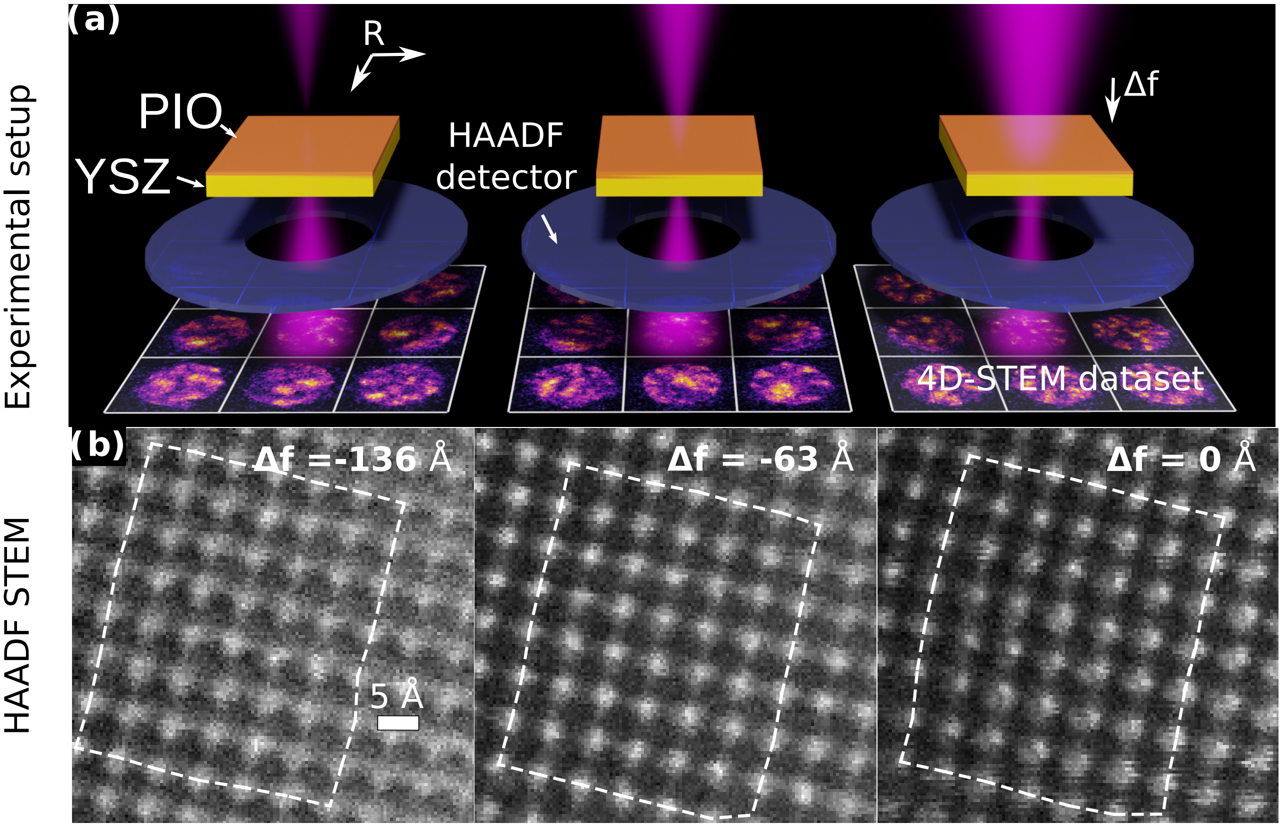

Fig. 2. (a) Recording of a 4D-STEM focal series for $\mathcal{S}$-matrix reconstruction. Simultaneously acquired HAADF STEM images are shown in (b).

4D-STEM dataset acquisition

For an experimental demonstration, we used a PIO layer grown on a (001)-oriented YSZ substrate by pulsed laser deposition at a growth temperature of 600 °C, wedge polished on the YSZ substrate side and then ion milled with a low-energy Ar^+ beam. Experiments were performed using the TEAM I instrument at the National Center for Electron Microscopy (NCEM) Facility of the Molecular Foundry, a double aberration-corrected Thermo-Fisher Titan 80-300. The instrument was operated with an accelerating voltage of 300 kV and a 20 mrad probe forming aperture. The reconstructed $\mathcal{S}$-matrix is sensitive to residual probe aberrations so careful initial alignment of the probe corrector and constant tuning of the stigmators before acquisition of 4D-STEM focal series was necessary to achieve good results. As shown in Fig. 2(a), a focal series of 4D-STEM data was recorded on a Gatan K3 direct-electron detector, operated in counting mode, at the end of a Gatan Continuum imaging filter with an energy slit width of 15 eV centered around the zero-loss peak. Three defocii of 0 Å, -63 Å and -136 Å relative to the entrance surface of the crystal were used, with the convention that a positive defocus means the beam comes to focus above the specimen surface. A probe step of 0.21 Å with probe dwell time of 0.874 ms and beam current of 2.01 pA (estimated using the K3 camera) was used. To maximise source coherence and minimize beam damage, source magnification (the “spot size” software setting) was set to 10, the penultimate setting. HAADF STEM images, from a detector inner angle of 110 mrad, recorded concurrently with the 4D-STEM data are shown in Fig. 2(a). Alignment of the frames in the focal series was achieved by fitting two-dimensional Gaussian functions to the atomic columns in the STEM HAADF images using the open-source Atomap package (Nord et al., 2017) to estimate the local deformation of the unit cell due to specimen drift and STEM scan distortion. Like the approach in Chen et al. (2016), the three closest Pb-Ir columns in the STEM HAADF image to any scan position then define an affine transform that maps the experimental probe position to its position in an idealized PIO unit cell. The scan-distortion corrected images in the focal series are then readily aligned. This is detailed in Fig. S1 of the supplementary material, the region that was input into the

$\mathcal{S}$-matrix reconstruction is shown with a dashed white outline in the HAADF STEM results in Fig. 2(b). Defocus values reported by the microscope software had to be adjusted by a multiplicative factor of 1.24, a value determined by comparing the geometric blur with defocus of gold nanoparticles embedded in amorphous carbon with the geometric blur expected from a 20 mrad probe forming aperture (see Fig. S2 of the supplementary material).

Results

$\mathcal{S}$-matrix depth sectioning results

The experimental $\mathcal{S}$-matrix was reconstructed using 10 iterations of the gradient descent algorithm described in Algorithm 1. Convergence with increasing iterations of the algorithm is shown in Fig. S3. Select components of the $\mathcal{S}$-matrix are shown in Fig. S4(a)-(e), and optical sectioning applied to the results. Optical sections at 100 Å intervals, reconstructed from the S-matrix components using the approach described in Materials and Methods section, are shown in Fig. 3(a)-(e). The -300 Å and 100 Å sections are outside the bounds of the object, though the lattice is still faintly visible. The visible lattice is a result attributable to a combination of the “Fourier image” effect described by Cowley & Moodie (1957) for coherent TEM images of periodic objects and blurring of the reconstruction in the z direction by the point-spread function of the experiment (Xin & Muller, 2009). The presence of Pb and Ir in the upper layers of the heterostructure is evidenced by appearance of “caldera” or volcano like atoms in Fig. 3(d). It is commonly seen in phase reconstructions in STEM that the phase imparted to an electron wave by high Z atomic columns, which strongly elastically and inelastically scatter the electron probe, are observed to underestimate the true scattering potential of an object leading to a dip in the reconstructed phase close to the atomic position (Close et al., 2015; Yang et al., 2017a). Thus the Pb and Ir atoms (Z=82 and Z=77) are observed to be darker in the reconstruction than the lighter Y and Zr atoms (Z=39 and Z=40). From the optical section we estimate the thickness to be 200 Å with a composition of approximately 50 Å of

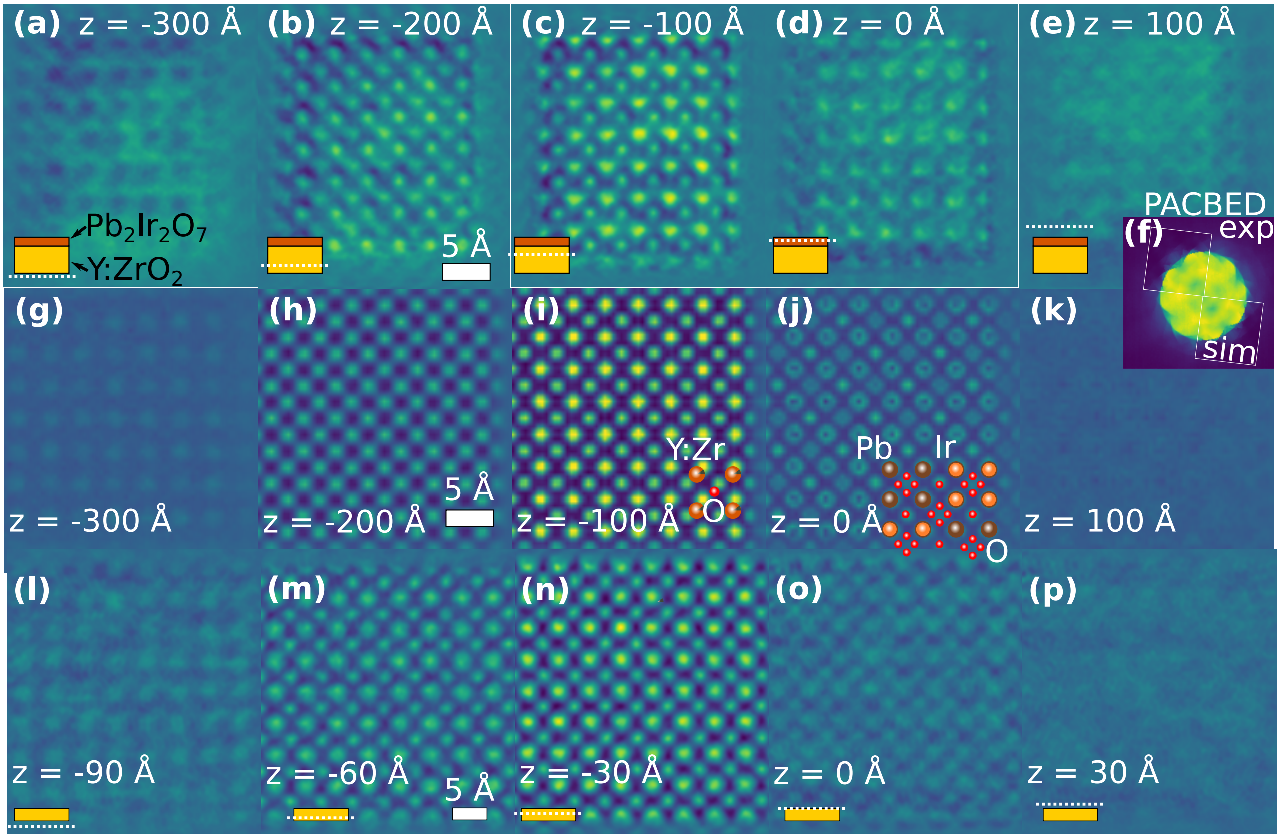

[t]

Fig. 3. Experimental reconstruction of the $\mathcal{S}$-matrix from a focal series of 4D-STEM scans of a PIO-YSZ heterostructure. The optical section reconstructed from experiment in Fig. 2 is shown in (a)-(e) with the 150 Å YSZ substrate visible in (b) and (c) and the 50 Å thick PIO layer visible in panel (d). An experimental and simulated position-averaged convergent beam electron diffraction (PACBED) pattern in (f) provides supporting evidence for the composition and structure implied by depth sectioning. Panels (g)-(k) are from a reconstruction from simulated data of such a structure. For reference, a similar $\mathcal{S}$-matrix depth section reconstructed from a 4D-STEM experiment with a ZrO only structure is shown in (l)-(p) and no “caldera” features to indicate Pb-Ir columns are evident.

PIO and 150 Å of YSZ. This is supported by comparison of the scan position-averaged convergent beam electron diffraction (PACBED) pattern (LeBeau et al., 2010) from experiment with that simulated for a model structure of PIO-YSZ of that thickness and composition of both materials in (f).

Fig. 3(g)-(k) shows the results of simulating and then reconstructing a model structure with 200 Å total thickness and containing 50 Å of PIO, and 150 Å of YSZ for equivalent focal conditions to the experimental data in Fig. 3(a)-(e). There is good overall qualitative agreement with experiment with the exception of the appearance of the oxygen columns which are alternately localized and de-localized in the PIO model, an effect which is visible in simulation, Fig. 3(j), but not in experiment, Fig. 3(d), a discrepancy that will be explored in detail later in the manuscript. Inclusion of defocus spread due to chromatic aberration (assuming a full-width at half-maximum probe energy spread of 0.8 eV, and lens Cc coefficient of 1.4 mm for the TEAM 1 instrument) was the most important experimental effect necessary to include in simulation for good agreement. As a demonstration how the appearance of caldera-like atoms is a signature of heavier atoms for this particular system, an experimental reconstruction from a different and much thinner region of the sample, free of PIO, is shown in Fig. 3(l)-(p). Caldera-like atoms are not visible at any of the slices of the reconstruction, nor in any of slices of a reconstruction from equivalent simulated dataset (not shown).

Reconstructions from phase-object based approaches

Phase reconstructions from single sideband (SSB) ptychography STEM, calculated from the 4D-STEM dataset, are shown in 4(a)-(c). As was the case with the $\mathcal{S}$-matrix reconstruction, SSB reveals the oxygen columns in the PIO-YSZ structure which are invisible in the HAADF STEM images of Fig. 2(b) and suggests, in the $\Delta f = 0$ Å image, that the dataset was recorded in a region of the specimen where the PIO layer terminates, with the upper left region of the image apparently only containing the YSZ substrate. The approximate boundary between these regions is indicated by a red dashed line in Fig. 4(c). This is consistent with the optical

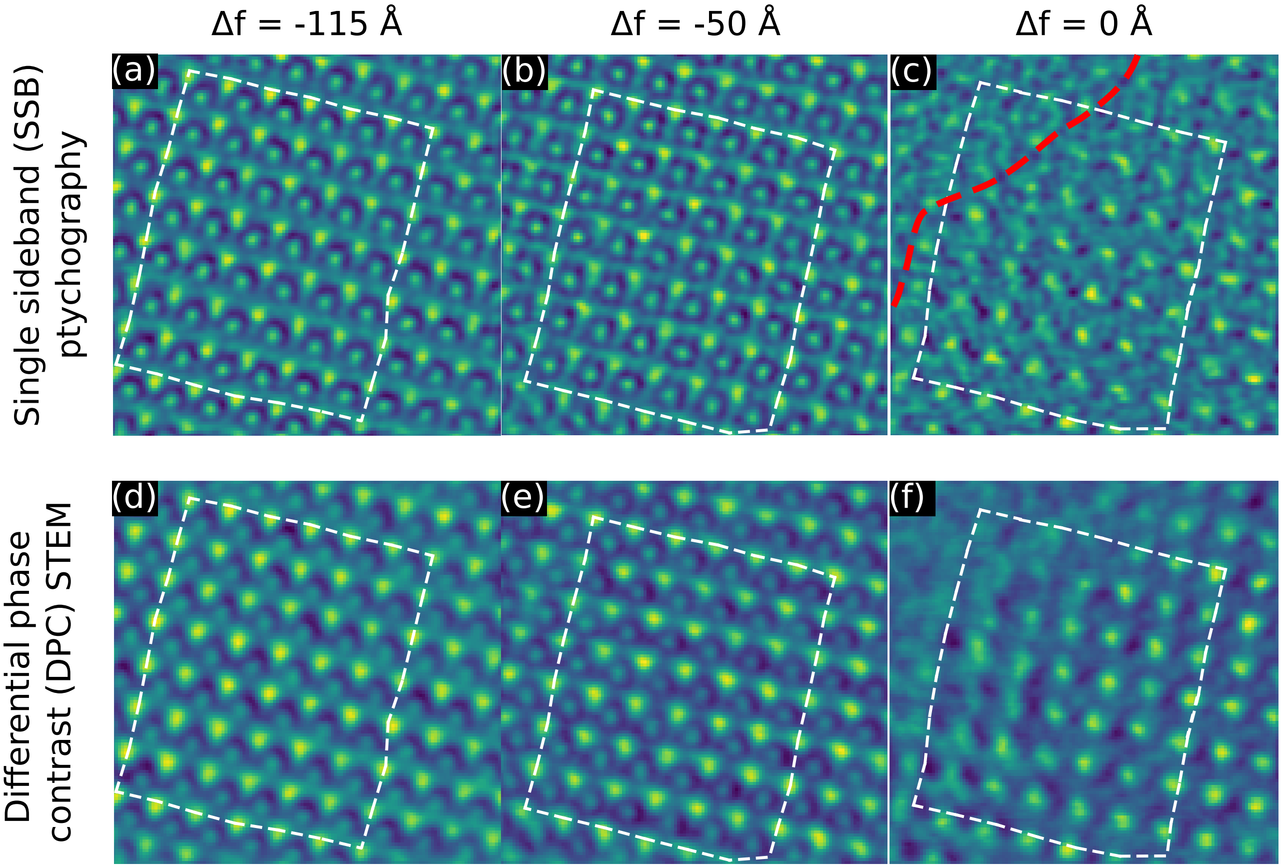

Fig. 4. Phase object approximation reconstructions of the experimental data from (a)-(c) single side band ptychography (SSB) (Rodenburg et al., 1993; Pennycook et al., 2015; Yang et al., 2016) and (d)-(f) differential phase contrast (DPC) STEM (Close et al., 2015; Shibata et al., 2017). These approaches generate broadly similar results and the PIO layer is visible in the right-most panel ($\Delta f = 0$ Å) (c) for SSB, where the approximate bounds of the PIO layer are indicated by a red dashed line, and (f) for DPC.

section in Fig. 3(d) showing stronger evidence of Pb and Ir atoms in the bottom right than in the upper left of the reconstruction. A differential phase contrast (DPC) STEM reconstruction of the datacube produces similar results to SSB ptychography, see Fig. 4(d)-(f).

Multislice ptychographic reconstruction

The electrostatic potential slices obtained by the multislice ptychographic reconstruction are shown in Fig. 5 for the 4D-STEM experimental dataset recorded simultaneous with the $\Delta f = 0$ Å HAADF-STEM image from Fig. 2(b). Optimization was done for 400 iterations, alternating between 2 iterations of potential update and 6 iterations of probe shape update, respectively. For the loss function, the ℓ_1 error metric was employed and no regularization used. The potential was reconstructed in 10 distinct planes seperated from one another by 25 Å in the z direction which are all displayed in Fig. 6(a)-(j). Results are broadly in agreement with the conclusions drawn from the $\mathcal{S}$-matrix, SSB and DPC-STEM analyses. The termination of the PIO flake is visible in the uppermost-slice of the reconstruction Fig. 5(a) and panels (b)-(i) are suggestive of a more uniform crystal lattice, showing that a single defocus reconstruction gives accurate 3D information about the crystal. Three seperate defoci were required to achieve comparable insights in Fig. 4 using SSB and DPC-STEM analyses.

The appearance of the cation columns is noticeably different within the PIO layers, Fig. 5(b) and (c), though this insight only seems well supported if the results of the other techniques employed within this paper are taken into account. Fig. 5 (h) and (i) also look noticeably distinct from the other planes, though we suspect that this is an artefact of reconstructing planes located far from the focal point of the STEM probe. The scattering of the probe is more strongly determined by atoms close to where the probe comes into focus than by planes where the probe has spread significantly. This becomes clearer when viewed alongside reconstructions from the other datasets in Fig. S5 of the supplementary material, reconstructed planes immediately below the focal plane in the multislice ptychography reconstruction are the sharpest and those far above or below the focal plane (± 150 Å) are significantly blurrier. To

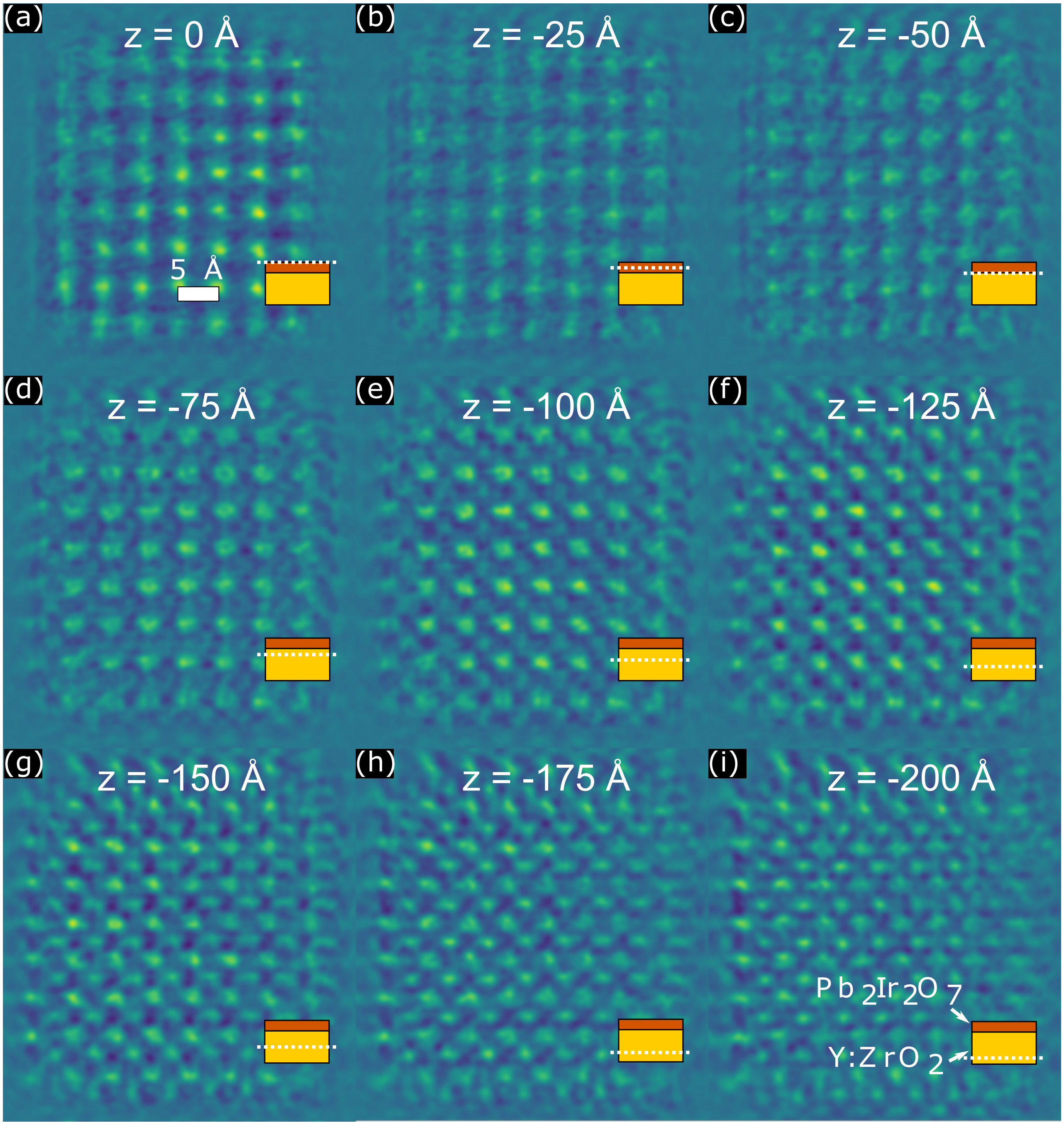

Fig. 5. Multislice ptychography reconstruction from the PIO- YSZ experimental dataset with defocus $\Delta f = 0$ Å with respect to the specimen surface. The termination of the PIO layer is evident in (a) whilst slices reconstructed from deeper within the crystal (b)-(j) suggest a uniform crystal lattice.

overcome this issue, multislice ptychography reconstruction algorithms should be designed to take into account datasets with multiple defoci as the $\mathcal{S}$ algorithm does and we highlight this as an area for future work. Though all the reconstruction techniques applied to the 4D-STEM dataset are supportive of similar conclusions, at present only the $\mathcal{S}$-matrix reconstruction gives definitive evidence of a PIO layer in the upper-layers of the volume due to the tell-tale "caldera" appearance of the Pb-Ir columns in the depth section.

Comments on the appearance of oxygen columns in the PIO structure

A final point to note is that PIO is a pyrochlore structure and, when projected down its [001] crystallographic zone-axis, the oxygen columns should exhibit alternating centered and delocalized columns, as shown in the structural overlay of Fig. 3(j). This was not visible in this reconstruction of the $Pb_2Ir_2O_7$ structure. The alternating delocalized O columns were also not visible in any of the annular bright-field (ABF) STEM images synthesized from the 4D-STEM datasets, e.g. see Fig. 6(a) for the dataset displayed in Fig. 3, which rules out the effect being an artefact of any of the reconstruction algorithms and makes it clear that this is a real feature of the as-prepared sample that requires some explanation.

To account for this, density functional theory (DFT) calculations were performed to determine the extent of compositional and structural influences on the oxygen positions. We use the parameter x to describe the position of O on the Wyckoff site $48f$ $(x,\frac{1}{8},\frac{1}{8})$ of the $Fd\overline{3}m$ (No. 227-2) space group, where x=0.375 gives a centered oxygen column and x=0.3125 is the maximum amount of oxygen off-centering allowed in the pyrochlore structure (Subramanian et al., 1983). Values of x for different structural variations are given in Table 1 (details in the supplementary material). Incorporating biaxial strain, stoichiometry variations (through the inclusion of oxygen vacancies) and an explicit YSZ/PIO interface do not cause significant changes in x. For 37.5% cation antisite defects, there is a considerable increase in x, indicating that a large proportion of antisite defects could induce a noticable change to the alternating pattern. Simulated STEM images of this amount of disorder are shown in Fig. 6(b)-(f). We see

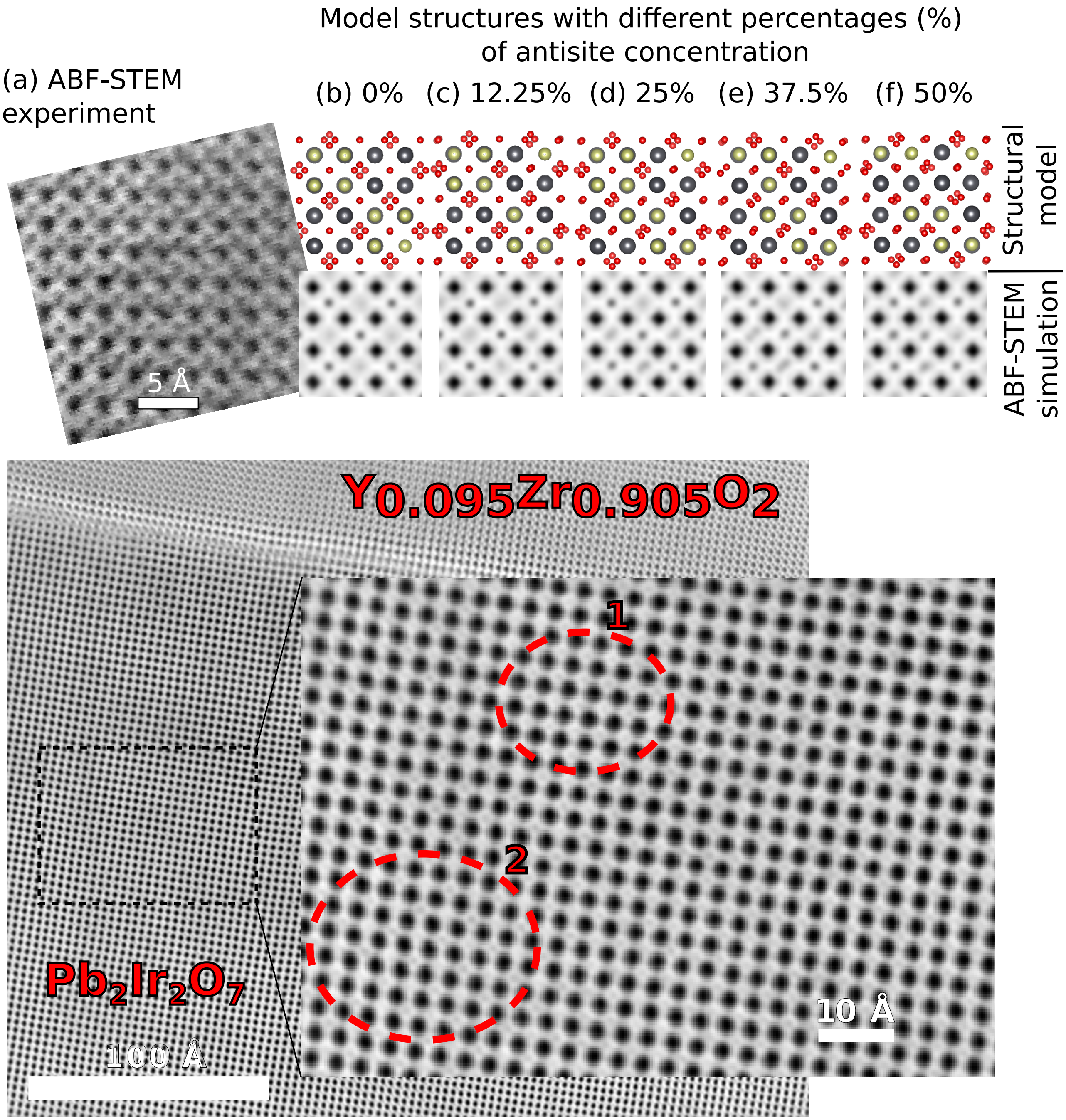

Fig. 6. The annular bright field (ABF) STEM image synthesised from the 4D-STEM dataset of Fig. 2 ($\Delta f = 0$ Å) lacks the alternating “splayed” and “tight” ordering of the oxygen columns that is predicted in the PIO pyrochlore structure in sub-figure (b). Increasing the amounts of cation disorder, (c) 12.25%, (d) 25%, (e) 37.5% and (f) 50% antisites per unit cell, disrupt the oxygen columns somewhat, though even with very high levels of disorder a satisfactory match with experiment is not achieved. Shown in (b) are ABF STEM images of a sample prepared in cross-section. In the zoomed view regions of alternating localized and delocalized oxygen columns are seen (e.g. region 2) as well as regions where the alternating localization and delocalization of the columns is not visible.

Structural variation	x
$Pb_2Ir_2O_7$	0.330
$Pb_2Ir_2O_7$ biaxially strained to 10.28 Å	0.332
PIO(001)/YSZ(001) interface	0.332
$Pb_2Ir_2O_{6.5}$	0.327-0.329
$Pb_2Ir_2O_6$	0.327
$Pb_2Ir_2O_7$ with % cation antisites,	average x
12.25%	0.336
25.0%	0.337
37.5%	0.344
50.0%	0.342

Table 1. Oxygen position parameter x, describing the oxygen column delocalization in the pyrochlore structure, calculated from DFT structural optimizations with strain, interface, and compositional variations.

that some individual oxygen columns are contracted. However, such a high proportion (37.5% and above) of cation antisite defects seem unlikely - we hypothesise that some smaller amount of antisite disorder is likely a factor contributing to the lack of localized-delocalized oxygen column ordering but cannot, on its own, fully explain the observed phenomenon. ABF-STEM images from a sample of the same material prepared such that the PIO-YSZ interface could be viewed in cross-section revealed regions where the alternating centered and delocalized oxygen columns were visible and areas where adjacent oxygen columns appeared to be centered, see Fig. 6(g). This suggests this alternating oxygen column order is likely present in nano-domains within the sample and cation disorder, either from the growth process or damage during imaging, results in alternating order and is not noticeable when the sample is viewed in plan-view projection in the electron microscope.

Conclusion

This paper has demonstrated a new electron microscopy technique capable of imaging light and heavy atoms in thicker, strongly scattering electron microscopy specimens using 4D-STEM data recorded in a single specimen orientation. For the case of the PIO-YSZ heterostructure we explored the visualisation of the PIO and YSZ layers using the $\mathcal{S}$-matrix technique. Existing alternatives to $\mathcal{S}$-matrix reconstruction and depth sectioning yield similar and supportive results though are not able, on their own, to give definitive evidence of the PIO layer.

Acknowledgements Work at the Molecular Foundry was supported by the Office of Science, Office of Basic Energy Sciences, of the U.S. Department of Energy under Contract No. DE-AC02-05CH11231. C.O. acknowledges support from the U.S. Department of Energy Early Career Research Program. J.C. and H.G.B. acknowledge support from the Presidential Early Career Award for Scientists and Engineers (PECASE) through the U.S. Department of Energy. S.M.G., E.S. and K.I. also acknowledge support from the Laboratory Directed Research and Development Program of LBNL under the U.S. Department of Energy Contract No. DE-AC02-05CH11231. E.S. acknowledges support from the US-Irish Fulbright Commission and work supported by the Air Force Office of Scientific Research under award number FA9550-18-1-0480. Computational resources were provided by the National Energy Research Scientific Computing Center and the Molecular Foundry. This research was partly supported under the Discovery Projects funding scheme of the Australian Research Council (Project No. FT190100619). M.S., T.C.P. and C.T.K acknowledge support from the Deutsche Forschungsgemeinschaft (DFG, German Research Foundation) - Project-ID 414984028 - SFB 1404.

All software used in this publication is available in the supplementary material. Due to their large size experimental datasets are not hosted along with the publication but can readily be made available upon request.

References

Allen, L.J., Faulkner, H.M.L. & Leeb, H. (2000). Inversion of dynamical electron diffraction data including absorption, *Acta Crystallographica Section A: Foundations of Crystallography* **56**, 119–126.

Bosch, E.G.T. & Lazić, I. (2019). Analysis of depth-sectioning STEM for thick samples and 3D imaging, *Ultramicroscopy* **207**, 112831.

Brown, H.G., Chen, Z., Weyland, M., Ophus, C., Ciston, J., Allen, L.J. & Findlay, S.D. (2018). Structure retrieval at atomic resolution in the presence of multiple scattering of the electron probe, *Physical Review Letters* **121**, 266102.

Chen, Z., Jiang, Y., Shao, Y.T., Holtz, M.E., Odstrčil, M., Guizar-Sicairos, M., Hanke, I., Ganschow, S., Schlom, D.G. & Muller, D.A. (2021). Electron ptychography achieves atomic-resolution limits set by lattice vibrations, *Science* **372**, 826–831.

Chen, Z., Weyland, M., Ercius, P., Ciston, J., Zheng, C., Fuhrer, M.S., D'Alfonso, A.J., Allen, L.J. & Findlay, S.D. (2016). Practical aspects of diffractive imaging using an atomic-scale coherent electron probe, *Ultramicroscopy* **169**, 107–121.

Ciston, J., Deng, B., Marks, L.D., Own, C.S. & Sinkler, W. (2008). A quantitative analysis of the cone-angle dependence in precession electron diffraction, *Ultramicroscopy* **108**, 514–522.

Close, R., Chen, Z., Shibata, N. & Findlay, S.D. (2015). Towards quantitative, atomic-resolution reconstruction of the electrostatic potential via differential phase contrast using electrons, *Ultramicroscopy* **159**, 124–137.

Coene, W. & Van Dyck, D. (1990). Inelastic scattering of high-energy electrons in real space, *Ultramicroscopy* **33**, 261–267.

Cowley, J.M. & Moodie, A.F. (1957). Fourier images: II-The out-of-focus patterns, *Proceedings of the Physical Society Section B* **70**, 497.

Donatelli, J.J. & Spence, J.C.H. (2020). Inversion of many-beam Bragg intensities for phasing by iterated projections: Removal of multiple scattering artifacts from diffraction data, *Physical Review Letters* **125**, 065502.

Findlay, S.D. (2005). Quantitative structure retrieval using scanning transmission electron microscopy, *Acta Crystallographica Section A: Foundations of Crystallography* **61**, 397–404.

Gao, S., Wang, P., Zhang, F., Martinez, G.T., Nellist, P.D., Pan, X. & Kirkland, A.I. (2017). Electron ptychographic microscopy for three-dimensional imaging, *Nature Communications* **8**, 1–8.

Guizar-Sicairos, M. & Fienup, J.R. (2008). Phase retrieval with transverse translation diversity: a nonlinear optimization approach, *Optics Express* **16**, 7264–7278.

Jiang, Y., Chen, Z., El Baggari, I., Kourkoutis, L.F., Elser, V. & Muller, D.A. (2018a). Breaking the Rayleigh limit in thick samples with multi-slice ptychography, *Microscopy and Microanalysis* **24**, 192–193.

Jiang, Y., Chen, Z., Han, Y., Deb, P., Gao, H., Xie, S., Purohit, P., Tate, M.W., Park, J., Gruner, S.M. et al. (2018b). Electron ptychography of 2D materials to deep sub-ångström resolution, *Nature* **559**, 343–349.

LeBeau, J.M., Findlay, S.D., Allen, L.J. & Stemmer, S. (2010). Position averaged convergent beam electron diffraction: Theory and applications, *Ultramicroscopy* **110**, 118–125.

Maiden, A.M., Humphry, M.J. & Rodenburg, J.M. (2012). Ptychographic transmission microscopy in three dimensions using a multi-slice approach, *JOSA A* **29**, 1606–1614.

Nellist, P.D., McCallum, B.C. & Rodenburg, J.M. (1995). Resolution beyond the “information limit” in transmission electron microscopy, *Nature* **374**, 630–632.

Nord, M., Vullum, P.E., MacLaren, I., Tybell, T. & Holmestad, R. (2017). Atomap: a new software tool for the automated analysis of atomic resolution images using two-dimensional Gaussian fitting, *Advanced Structural and Chemical Imaging* **3**, 9.

Oh, M.H., Cho, M.G., Chung, D.Y., Park, I., Kwon, Y.P., Ophus, C., Kim, D., Kim, M.G., Jeong, B., Gu, X.W. et al. (2020). Design and synthesis of multigrain nanocrystals via geometric misfit strain, *Nature* **577**, 359–363.

Ophus, C. (2019). Four-dimensional scanning transmission electron microscopy (4D-STEM): from scanning nanodiffraction to ptychography and beyond, *Microscopy and Microanalysis* **25**, 563–582.

Ophus, C., Harvey, T.R., Yasin, F.S., Brown, H.G., Pelz, P.M., Savitzky, B.H., Ciston, J. & McMorran, B.J. (2019). Advanced phase reconstruction methods enabled by four-dimensional scanning transmission electron microscopy, *Microscopy and Microanalysis* **25**, 10–11.

Pelz, P.M., Brown, H.G., Stonemeyer, S., Findlay, S.D., Zettl, A., Ercius, P., Zhang, Y., Ciston, J., Scott, M.C. & Ophus, C. (2021). Phase-contrast imaging of multiply-scattering extended objects at atomic resolution by reconstruction of the scattering matrix, *Physical Review Research* **3**, 023159.

Pennycook, T.J., Lupini, A.R., Yang, H., Murfitt, M.F., Jones, L. & Nellist, P.D. (2015). Efficient phase contrast imaging in STEM using a pixelated detector. Part 1: Experimental demonstration at atomic resolution, *Ultramicroscopy* **151**, 160–167.

Rodenburg, J.M., McCallum, B.C. & Nellist, P.D. (1993). Experimental tests on double-resolution coherent imaging via stem, *Ultramicroscopy* **48**, 304–314.

Schloz, M., Pekin, T.C., Chen, Z., den Broek, W.V., Muller, D.A. & Koch, C.T. (2020). Overcoming information reduced data and experimentally uncertain parameters in ptychography with regularized optimization, *Opt Express* **28**, 28306–28323.

Shibata, N., Kohno, Y., Findlay, S.D., Sawada, H., Kondo, Y. & Ikuhara, Y. (2010). New area detector for atomic-resolution scanning transmission electron microscopy, *Journal of Electron Microscopy* **59**, 473–479.

Shibata, N., Seki, T., Sánchez-Santolino, G., Findlay, S.D., Kohno, Y., Matsumoto, T., Ishikawa, R. & Ikuhara, Y. (2017). Electric field imaging of single atoms, *Nature Communications* **8**, 1–7.

Spence, J.C.H. (1998). Direct inversion of dynamical electron diffraction patterns to structure factors, *Acta Crystallographica Section A: Foundations of Crystallography* **54**, 7–18.

Sturkey, L. (1962). The calculation of electron diffraction intensities, *Proceedings of the Physical Society* **80**, 321.

Subramanian, M., Aravamudan, G. & Subba Rao, G. (1983). Oxide pyrochlores — A review, *Progress in Solid State Chemistry* **15**, 55–143.

Thibault, P. & Guizar-Sicairos, M. (2012). Maximum-likelihood refinement for coherent diffractive imaging, *New J Phys* **14**, 063004.

van Benthem, K., Lupini, A.R., Oxley, M.P., Findlay, S.D., Allen, L.J. & Pennycook, S.J. (2006). Three-dimensional ADF imaging of individual atoms by through-focal series scanning transmission electron microscopy, *Ultramicroscopy* **106**, 1062–1068.

Wang, G., Giannakis, G.B. & Eldar, Y.C. (2017). Solving systems of random quadratic equations via truncated amplitude flow, *IEEE Transactions on Information Theory* **64**, 773–794.

Weinberg, S. (1995). *The quantum theory of fields*, vol. 2, Cambridge university press.

Withers, F., Del Pozo-Zamudio, O., Mishchenko, A., Rooney, A.P., Gholinia, A., Watanabe, K., Taniguchi, T., Haigh, S.J., Geim, A., Tartakovskii, A.I. et al. (2015). Light-emitting diodes by band-structure engineering in van der waals heterostructures, *Nature Materials* **14**, 301–306.

Xin, H.L. & Muller, D.A. (2009). Aberration-corrected ADF-STEM depth sectioning and prospects for reliable 3D imaging in S/TEM, *Journal of Electron Microscopy* **58**, 157–165.

Yadav, A., Nelson, C., Hsu, S., Hong, Z., Clarkson, J., Schlepütz, C., Damodaran, A., Shafer, P., Arenholz, E., Dedon, L. et al. (2016). Observation of polar vortices in oxide superlattices, *Nature* **530**, 198–201.

Yang, H., MacLaren, I., Jones, L., Martinez, G.T., Simson, M., Huth, M., Ryll, H., Soltau, H., Sagawa, R., Kondo, Y. et al. (2017a). Electron ptychographic phase imaging of light elements in crystalline materials using wigner distribution deconvolution, *Ultramicroscopy* **180**, 173–179.

Yang, H., Rutte, R., Jones, L., Simson, M., Sagawa, R., Ryll, H., Huth, M., Pennycook, T., Green, M., Soltau, H. et al. (2016). Simultaneous atomic-resolution electron ptychography and Z-contrast imaging of light and heavy elements in complex nanostructures, *Nature Communications* **7**, 1–8.

Yang, Y., Chen, C.C., Scott, M., Ophus, C., Xu, R., Pryor, A., Wu, L., Sun, F., Theis, W., Zhou, J. et al. (2017b). Deciphering chemical order/disorder and material properties at the single-atom level, *Nature* **542**, 75–79.